Synthesis-Dependent First-Order Raman Scattering in $SrTiO_3$ Nanocubes at Room Temperature

Federico A. Rabuffetti,[†,‡] Hack-Sung Kim,[†,‡,§] James A. Enterkin,[†,‡] Yingmin Wang,[‡,||] Courtney H. Lanier,[‡,||] Laurence D. Marks,[‡,||] Kenneth R. Poeppelmeier,[†,‡] and Peter C. Stair*[,†,‡,§]

Department of Chemistry, Department of Materials Science and Engineering, and Institute for Catalysis in Energy Processes, Northwestern University, Evanston, Illinois 60208, and Division of Chemical Sciences and Engineering, Argonne National Laboratory, Argonne, Illinois 60439

Received April 30, 2008. Revised Manuscript Received June 3, 2008

Raman spectroscopy was used to demonstrate that the lattice dynamics of $SrTiO_3$ (STO) nanoparticles strongly depends on their microstructure, which is in turn determined by the synthetic approach employed. First-order Raman modes are observed at room temperature in STO single-crystalline nanocubes with average edge lengths of 60 and 120 nm, obtained via sol-precipitation coupled with hydrothermal synthesis and a molten salt procedure, respectively. First-order Raman scattering arises from local loss of inversion symmetry caused by surface frozen dipoles, oxygen vacancies, and impurities incorporated into the host lattice. The presence of polar domains is suggested by the pronounced Fano asymmetry of the peak corresponding to the TO2 polar phonon, which does not vanish at room temperature. These noncentrosymmetric domains will likely influence the dielectric response of these nanoparticles.

Introduction

Owing to its high dielectric constant, large dielectric tunability, and low microwave losses, $SrTiO_3$ (STO) has attracted increasing interest as a candidate material for tunable microwave devices operating at cryogenic temperatures.[1,2] However, STO thin films, required for device applications, exhibit reduced dielectric permittivity and dielectric losses an order of magnitude higher than single crystals.[3,4] Dielectric properties of STO thin films have also been reported to be highly dependent on the film thickness, epitaxy, and film microstructure.[5]

To achieve a comprehensive understanding of structure−property relationships in ferroelectric and incipient ferroelectric thin films, the study of phonon dynamics is of major significance. Raman spectroscopy has proved to be an invaluable tool to study the lattice dynamics of these systems, because of its sensitivity to short-range distortions arising from microstructural defects. Nanoparticles of ferroelectric and incipient ferroelectric perovskites constitute new systems in which to study structure−property relationships. Recent advances in the synthesis of perovskite nanoparticles[6–15] have led to renewed interest in understanding how their dielectric properties differ from bulk and thin film specimens. Recently, Banerjee and co-workers[16] reported a Raman study on STO nanocubes obtained via a molten salt procedure.

In this paper, we report a temperature-dependent Raman study, in the range 85−300 K, of STO single-crystalline nanocubes obtained via a molten salt procedure and a sol-precipitation coupled with hydrothermal treatment method. Polycrystalline STO synthesized using conventional solid state reaction was also investigated; the corresponding results are reported for comparison. Our findings are discussed in the context of previous investigations of phonon dynamics in STO single crystals and thin films.

Experimental Section

Sample Preparation. *Solid-State Reaction (SSR).* Polycrystalline STO powder was obtained through solid state reaction by mixing

* To whom correspondence should be addressed. E-mail: pstair@northwestern.edu.
† Department of Chemistry, Northwestern University.
‡ Institute of Catalysis and Energy Processes, Northwestern University.
§ Division of Chemical Sciences and Engineering, Argonne National Laboratory.
|| Department of Materials Science and Engineering, Northwestern University.

(1) Vendik, O. G.; Hollmann, E. K.; Kozyrev, A. B.; Prudan, A. M. *J. Supercond.* **1999**, *12* (2), 325–338.
(2) Xi, X. X.; Li, H.-Ch.; Si, W.; Sirenko, A. A.; Akimov, I. A.; Fox, J. R.; Clark, A. M. *J. Electroceram.* **2000**, *4* (2−3), 393–405.
(3) Zhou, C.; Newns, D. M. *J. Appl. Phys.* **1997**, *82* (6), 3081–3088.
(4) Li, H.-Ch.; Si, W.; West, A. D.; Xi, X. X. *Appl. Phys. Lett.* **1998**, *73* (4), 464–466.
(5) Ostapchuk, T.; Petzelt, J.; Železný, V.; Pashkin, A.; Pokorný, J.; Drbohlav, I.; Kužel, R.; Rafaja, D.; Gorshunov, B. P.; Dressel, M.; Ohly, Ch.; Hoffmann-Eifert, S.; Waser, R. *Phys. Rev. B* **2002**, *66*, 235–406, and references therein.
(6) Mao, Y. B.; Banerjee, S. S.; Wong, S. S. *J. Am. Chem. Soc.* **2003**, *125* (51), 15718–15719.
(7) Wu, X.; Wu, D.; Liu, X. *Solid State Commun.* **2008**, *145*, 255–258.
(8) Balaya, P.; Ahrens, M.; Kienle, L.; Maier, J.; Rahmati, B.; Bo Lee, S.; Sigle, W.; Pashkin, A.; Kuntscher, C.; Dressel, M. *J. Am. Ceram. Soc.* **2006**, *89* (9), 2804–2811.
(9) Zheng, H.; Liu, X.; Meng, G.; Toft, O. T. *J. Mater. Sci.: Mater. Electron.* **2001**, *12* (11), 629–635.
(10) Calderone, V. R.; Testino, A.; Buscaglia, M. T.; Bassoli, M.; Bottino, C.; Viviani, M.; Buscaglia, V.; Nanni, P. *Chem. Mater.* **2006**, *18* (6), 1627–1633.
(11) Moon, J.; Kerchner, J. A.; Krarup, H.; Adair, J. H. *J. Mater. Res.* **1999**, *14* (2), 425–435.
(12) Um, M.-H.; Kumazawa, H. *J. Mater. Sci.* **2000**, *35*, 1295–1300.
(13) Zhang, S.; Liu, J.; Han, Y.; Chen, B.; Li, X. *Mater. Sci. Eng., B* **2004**, *110*, 11–17.
(14) Herrig, H.; Hempelmann, R. *Mater. Lett.* **1996**, *27*, 287–292.
(15) Ahmad, T.; Ganguli, A. K. *J. Am. Ceram. Soc.* **2006**, *89* (4), 1326–1332.
(16) Banerjee, S.; Kim, D.-I.; Robinson, R. D.; Herman, I. P.; Mao, Y.; Wong, S. S. *Appl. Phys. Lett.* **2006**, *89*, 223130.

10.1021/cm801192t CCC: $40.75
Published on Web 08/07/2008

stoichiometric amounts of SrC_2O_4 (97%, Aldrich) and TiO_2 anatase (99.9%, Aldrich). The mixture was ground in an agate mortar, placed into an alumina crucible, and finally heated in air at 1523 K for 3.5 h.

Molten Salt Synthesis (MSS). STO nanoparticles were synthesized via a molten salt procedure similar to that described by Mao et al.[6] Briefly, SrC_2O_4 (97%, Aldrich), TiO_2 anatase (99.9%, Aldrich), and NaCl (99.5%, Fisher) in a 1:1:20 molar ratio were mixed and ground in an agate mortar. In contrast to the synthetic procedure proposed by Mao and co-workers, the nonionic surfactant NP-9 was not employed in this work. The mixture was loaded into an alumina crucible and heated in air at 1093 K for 3.5 h. The resulting powder was washed thoroughly with double-deionized water, and dried in an oven at 363 K for 24 h; this specimen is designated as MSS-1 STO. A second sample, labeled MSS-2 STO, was synthesized following the same procedure, but two slight variations were introduced: (1) the Sr:Ti:NaCl molar ratio in the starting mixture was 3:2:20, and (2) after reaction at 1093 K the resulting powder was washed, first with CH_3COOH to remove the $SrCO_3$ resulting from the use of an excess of Sr and then with double-deionized water.

Sol-Precipitation—Hydrothermal Synthesis (HTS). Additionnally, STO nanoparticles were synthesized via sol-precipitation followed by hydrothermal treatment. Two solutions, designated A and B, containing the Sr and Ti precursors, respectively, were prepared. Solution A was prepared by dissolving 2.4313 g of $Sr(OH)_2 \cdot 8H_2O$ (Alfa Aesar, 99%) in 50 mL of 1 M acetic acid yielding a clear transparent solution with pH ~4. Solution B was prepared by adding 1.00 mL of $TiCl_4$ (Acros Organics, 99.9%) to 20 mL of absolute ethanol yielding a light yellow transparent solution with pH ~1. Solution B was added to solution A under moderate stirring resulting in a clear transparent solution with pH ~1; the Sr:Ti molar ratio in this solution was equal to 1. Coprecipitation of $SrTiO_3$ was then induced by adding 5 g of NaOH pellets (Mallinckrodt Chemicals, 99%) to the above precursor solution while maintaining stirring. Upon dissolution of the NaOH pellets, the solution became progressively cloudy; a continuous increase of viscosity was observed until a white opaque gel was formed. After vigorous stirring, the gel lost rigidity and a highly viscous suspension with pH ~14 was obtained, which was stirred moderately for 10 min. The suspension was loaded into a 125 mL Teflon-lined autoclave and heated at 240 °C for 24 h. The autoclave was subsequently allowed to cool to room temperature. The solution was filtered and the product (white powder) washed thoroughly with double-deionized water, and air-dried at 80 °C for 24 h.

Sample Characterization. *X-ray Diffraction.* X-ray diffraction (XRD) patterns were collected in the 2θ range 20−80° using a Rigaku DMAX diffractometer in the Bragg−Brentano configuration operated at 20 mA and 40 kV. Cu Kα radiation ($\lambda = 1.5418$ Å) filtered with Ni was employed. The step size and collection time were 0.025° and 1 s per step, respectively.

Transmission Electron Microscopy and Electron Diffraction. Transmission electron microscopy (TEM) and high-resolution TEM (HRTEM) images, as well as selected area electron diffraction (SAED) patterns, were obtained using a JEOL JEM-2100F electron microscope operated at 200 kV with energy dispersive X-ray analysis (EDXS) capabilities. Specimens for such studies were prepared using a two-step procedure. First, a tiny amount of sample was dispersed in methanol and sonicated for 10 min. A drop of the resulting suspension was then deposited onto a 400 mesh Cu grid coated with a Lacey carbon film. An identical preparation procedure was followed for each sample.

Raman Spectroscopy. Raman spectra were recorded with a triple spectrometer (Princeton Instruments Acton, Trivista 555) equipped with a liquid nitrogen-cooled CCD detector using 488.0 nm radiation from an Ar^+ laser for excitation. The laser power delivered to the sample was about 2.5 mW. An ellipsoidal mirror was used to collect and focus the scattered light into the spectrometer. Raman spectra at temperatures below 300 K were obtained using a custom-made Raman cell where liquid nitrogen passes through a tube located below the samples. A K-type thermocouple in contact with the sample holder in the Raman cell was used for the temperature measurement. Cyclohexane, trichloroethylene, sulfur, and polystyrene were used as frequency standards for calibration of Raman shifts. The absolute accuracy of Raman shifts is estimated to be ± 1 cm^{-1}. The spectral resolution was 4 cm^{-1}.

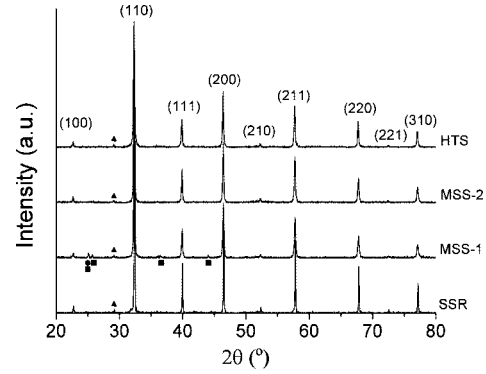

Figure 1. XRD patterns of SSR, MSS-1, MSS-2, and HTS STO samples. Peaks corresponding to secondary phases present in MSS-1 STO are denoted by solid symbols: ■, $SrCO_3$; ●, TiO_2. The peak labeled with ▲ corresponds to Cu Kβ.

Results and Discussion

X-ray Diffraction Analysis. X-ray diffraction patterns of the as-prepared powders are shown in Figure 1. SSR STO exhibits a trace amount of a secondary phase as indicated by the two small peaks on both sides of the (110) reflection; since the presence of this phase does not affect the results presented in this work, it will be no longer considered. MSS-1 STO contains $SrCO_3$ and TiO_2 as secondary phases, whereas MSS-2 and HTS STO samples are single phase. For all four samples, all peaks corresponding to the perovskite phase can be indexed to the cubic space group $Pm\bar{3}m$ with lattice constant $a \approx 3.90$ Å (PDF File No. 84−0444). No splitting of the (100), (110), and (200) reflections is observed in the XRD patterns of SSR, MSS-1, MSS-2, and HTS STO; hence, according to XRD, none of these structures show evidence of a tetragonal distortion.

Transmission Electron Microscopy and Electron Diffraction. TEM images of SSR, MSS-1, MSS-2, and HTS STO samples are shown in Figures 2, 3, 4, and 5, respectively.

SSR STO particles do not exhibit regular shape. The average particle size can be estimated to be ~0.8 μm. Very large (1−2 μm) agglomerates are observed.

MSS-1 and MSS-2 STO nanoparticles are cubic shaped with well defined edges of average length ~120 nm (Figures 3 and 4); for STO nanocubes synthesized via molten salt, Mao et al.[6] reported an average size of 80 nm. According to electron diffraction (see Figures 3c and 4c), the nanoparticles are single-crystalline in both samples. Although these powders are not agglomerate-free, interparticle agglomeration is greatly reduced compared to SSR STO. For STO, the

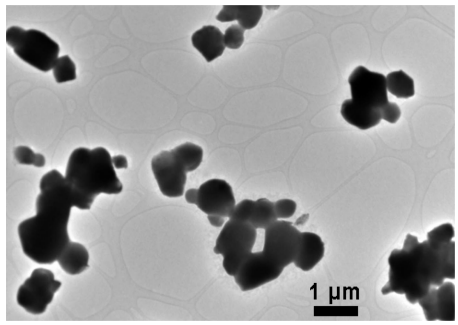

Figure 2. TEM image of SSR STO microcrystalline grains.

{001} faces have the lowest energy and therefore it is expected that these nanocubes have these faces primarily exposed. In addition, small {110} facets are clearly seen in some nanoparticles belonging to the MSS-2 STO sample (Figure 4b). The stabilization of the {110} faces at high temperatures has been observed in STO single crystals.[17]

HTS STO nanoparticles exhibit very regular and uniform cubic shape with rounded edges of average length 60 nm and well-defined faces, as well as surface steps (Figure 5); no significant agglomeration of the particles was observed for this sample. Qualitative EDXS analysis does not reveal the presence of any other elements than Sr and Ti. In addition, STO nanocubes appear single-crystalline to electron diffraction and HRTEM imaging: all the spots in the diffraction pattern can be indexed to a cubic perovskite structure, and the spacing of the lattice fringes corresponding to the {110} planes equals 2.76 Å which corresponds to a lattice constant $a \approx 3.90$ Å, in agreement with XRD data. These fringes make an angle of 45° with the edge of the nanocube, and go across the nanocrystal undistorted. A striking feature of HTS STO nanocubes is the presence, within the nanocrystallite, of numerous circular- and square-shaped features with sizes ranging from 5 to 25 nm (Figure 6). Square-shaped features exhibit lower contrast and a remarkable similarity and alignment with the cubic structure of the nanoparticle, i.e., well-defined edges parallel to the nanoparticle edges, and rounded vertices. High-angle tilting TEM imaging further showed that the depth of these structures approximately matches their lateral size, i.e. they are cubic-shaped, and that they are not connected to the outer surface of the nanoparticle. Electron energy loss spectroscopy (EELS) thickness mapping analysis revealed a depletion of material across the cubic-shaped structures, suggesting the presence of cavities within the nanocrystallite. Cubic-shaped cavities, although smaller in size, have been observed in nanocrystalline STO prepared via a modified peroxy-based route, by Balaya and co-workers.[8] In addition, areas of lower thickness contrast have been observed in STO nanoparticles grown by epitaxial self-assembly from an aqueous gel suspension by Calderone et al., who ascribed them to the presence of nanosized cavities between the self-assembled primary crystallites.[10]

Raman Spectroscopy. Raman spectra of SSR, MSS-1, MSS-2, and HTS STO collected over the temperature range 85−300 K are depicted in Figures 7a-d. Phonon frequencies reported in previous investigations[18–20] of STO are summarized in Table 1.

At room temperature, STO has an a ideal cubic perovskite structure with space group $Pm\bar{3}m$. Because all the zone-center optical phonons are of odd symmetry, no first-order Raman activity is expected on the basis of factor group symmetry analysis; instead, the room temperature spectrum should be dominated by second-order scattering.[21,22] The Raman spectrum of SSR STO at room temperature agrees well with these predictions and with previously reported spectra.[19,22–27] It consists of a low-frequency band at 79 cm^{-1} and two second-order broad bands centered in the 200−400 and 600−800 cm^{-1} regions. The assignments proposed by previous authors[21,22,26] for the two broad bands are in good agreement with our data. Only additive combinations and overtones contribute to the bands at 251, 623, 688, and 721 cm^{-1}, since their intensities do not decrease upon cooling. In contrast, difference combinations contribute to the bands at 303 and 363 cm^{-1}, as their intensities decrease with decreasing temperature causing a reduction of the band contour around 300−400 cm^{-1}. These two bands do not disappear upon cooling because additive combinations and overtones also contribute to them.

The band at 79 cm^{-1} shifts to lower frequencies upon cooling, to 72 cm^{-1} at 85 K. A similar band centered at ~80 cm^{-1} has been observed in previous Raman investigations of STO single crystals[22–25] and polycrystalline samples[19,26] and was assigned to a difference combination process, as its intensity was observed to decrease upon cooling. In our case, no major changes in the intensity of this band are noticeable, at least down to 85 K; therefore, it cannot be assigned a priori to a difference process. Moreover, because SSR STO does not exhibit first-order Raman peaks at room temperature, it cannot correspond to a fundamental of the TO1 phonon because its activation is symmetry-forbidden. Perry et al.[21] observed a similar band and assigned it to an overtone of the TO1 phonon but not located at the zone center. A similar assignment fits our experimental data; nevertheless, measurements extended down to liquid He temperatures are required to assign this band conclusively.

Raman spectra of MSS-1, MSS-2, and HTS STO samples, display several interesting features beyond second-order bands. At room temperature, the spectrum corresponding to MSS-1 STO shows four additional peaks at 146, 176, 543,

(17) Erdman, N.; Marks, L. D. *Surf. Sci.* **2003**, *526*, 107–114.
(18) Stirling, W. G. *J. Phys. C: Solid State Phys.* **1972**, *5*, 2711–2730.
(19) Petzelt, J.; Ostapchuk, T.; Gregora, I.; Rychetský, I.; Hoffmann-Eifert, S.; Pronin, A. V.; Yuzyuk, Y.; Gorshunov, B. P.; Kamba, S.; Bovtun, V.; Pokorný, J.; Savinov, M.; Porokhonskyy, V.; Rafaja, D.; Vanek, P.; Almeida, A.; Chaves, M. R.; Volkov, A. A.; Dressel, M.; Waser, R. *Phys. Rev. B* **2001**, *64*, 184111.
(20) Vogt, H.; Neumann, G. *Phys. Status Solidi B* **1979**, *92*, 57–63.
(21) Perry, C. H.; Fertel, J. H.; McNelly, T. F. *J. Chem. Phys.* **1967**, *47* (5), 1619–1625.
(22) Nilsen, W. G.; Skinner, J. G. *J. Chem. Phys.* **1968**, *48* (5), 2240–2248.
(23) Schaufele, R. F.; Weber, M. J. *J. Chem. Phys.* **1967**, *46*, 2859–2861.
(24) Fleury, P. A.; Worlock, J. M. *Phys. Rev.* **1968**, *174* (2), 613–623.
(25) Taylor, W.; Murray, A. F. *Solid State Commun.* **1979**, *31*, 937–944.
(26) Balachandran, U.; Eror, N. G. *Commun. Am. Ceram. Soc.* **1982**, 54–56.
(27) Ouillon, R.; Pinan-Lucarre; J, P.; Ranson, P.; Pruzan, Ph.; Mishra, S. K.; Ranjan, R.; Pandey, D. *J. Phys.: Condens. Matter.* **2002**, *14*, 2079–2092.

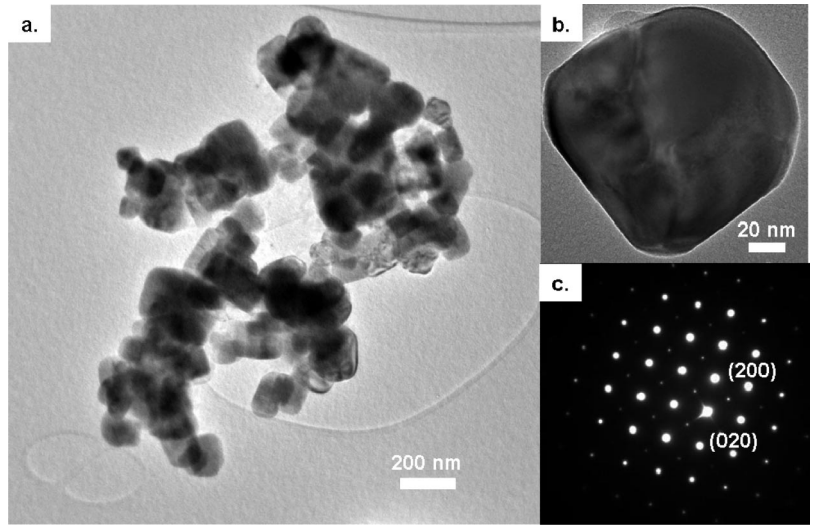

Figure 3. (a) TEM image of MSS-1 STO nanocubes; (b) TEM image of a single nanocube; and (c) corresponding SAED pattern along the [001] zone axis. The weaker spots arise from the difference in atomic scattering factors of Sr and Ti.

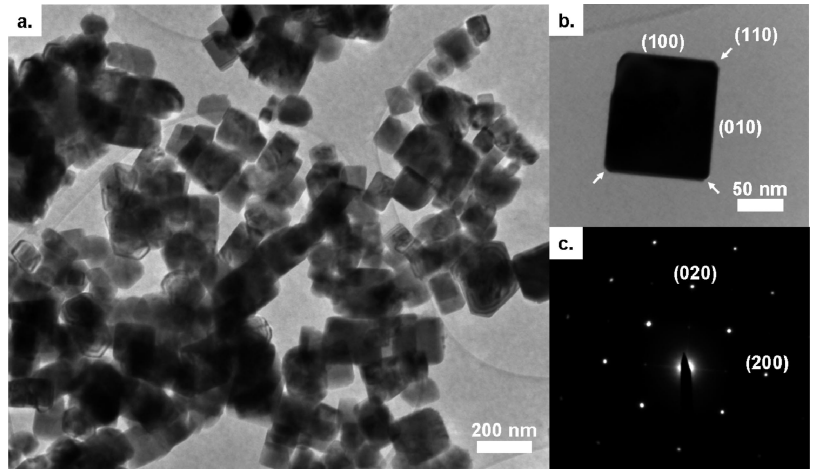

Figure 4. (a) TEM image of MSS-2 STO nanocubes; (b) TEM image of a single nanocube exhibiting large {100} and small {110} facets (denoted by arrows); and (c) corresponding SAED pattern along the [001] zone axis.

and 797 cm^{-1}. Raman spectra of MSS-2 and HTS STO samples display the same peaks with the exception of the one at 146 cm^{-1}. In addition, two weak peaks at 271 and 476 cm^{-1} are observable in the spectrum of HTS STO nanocubes. The intensity of these additional peaks relative to the second-order bands increases upon cooling. In fact, for both MSS-1 and MSS-2 STO specimens, a weak peak at 267 cm^{-1} and a shoulder at 476 cm^{-1} show up at 168 K and are clearly seen at 85 K. Also, two bands at 545 and 794 cm^{-1} are observed in the spectrum of SSR STO at 208 K, becoming more intense as temperature decreases to 85 K. Inspection of Table 1 shows an excellent match between the Raman shift of peaks at ~176, 267, 476, 545, and 795 cm^{-1} and the frequencies of TO2, TO3, LO3, TO4, and LO4 phonons, respectively. This demonstrates that these bands arise from first-order Raman scattering from STO vibrational modes. Recently, Banerjee et al.[16] observed strong first-order Raman activity at room temperature in 80 nm STO nanocubes synthesized via molten salt. Their observations agree with the results presented here, except that no peaks at ~267 and 476 cm^{-1} are reported at low temperatures, and the strong feature at ~795 cm^{-1} was not observed because it was out of their measurement range.

First-order Raman activity is expected for STO at temperatures below 110 K, where the structure is tetragonal with space-group *I*4/*mcm*.[24,28] Tetragonal STO has seven Raman-active modes including two pairs of degenerate $\{E_g, B_{1g}\}$ modes and a B_{2g} mode; their corresponding Raman bands have been observed in the ranges 140−150,[19,22–27] 440−460,[19,22–27] and 220−260 cm^{-1},[19,24–27] respectively. Banerjee and co-workers[16] observed a strong peak at ~145 cm^{-1} in the Raman spectrum of STO nanocubes, which they assigned to the E_g mode. We found the presence of this peak to be strongly dependent on the content of $SrCO_3$ of the sample; the Raman spectrum of $SrCO_3$ is shown in Figure 8. According to XRD and Raman spectroscopy, MSS-1 STO contains significant amounts of $SrCO_3$; however, neither of these techniques detect $SrCO_3$ in MSS-2 and only traces are detected by Raman spectroscopy in HTS STO. No peak at 146 cm^{-1} is observed for $SrCO_3$-free samples. Because

(28) Fleury, P. A.; Scott, J. F.; Worlock, J. M. *Phys. Rev. Lett.* **1968**, *21* (1), 16–19.

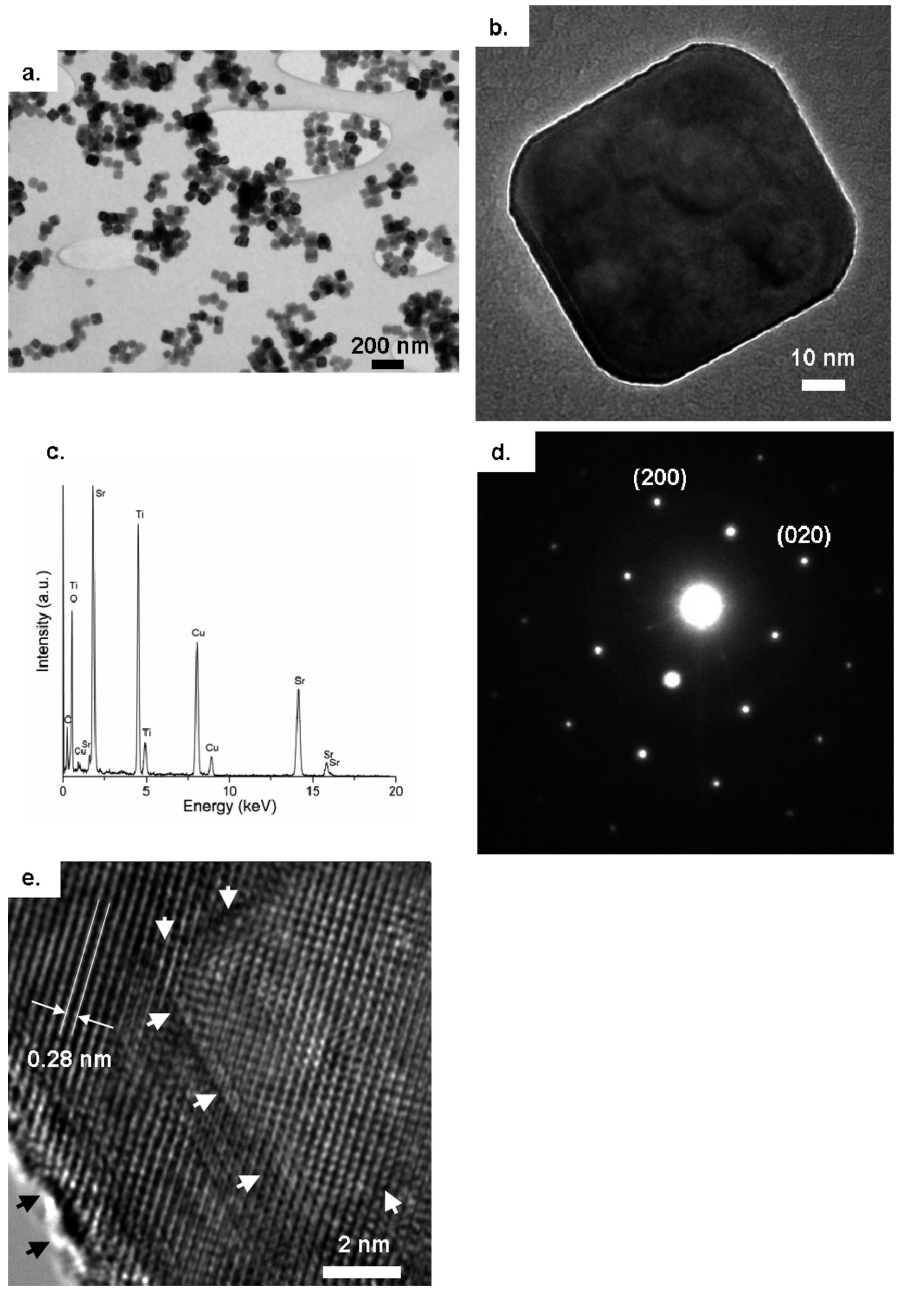

Figure 5. (a) TEM image of HTS STO nanocubes; (b) TEM image of a single nanocube; (c) corresponding EDXS spectrum, and (d) SAED pattern along the [001] zone axis; (e) HRTEM image of the lattice fringes corresponding to the {110} planes; white arrows depict a cubic-shaped structure within the nanocrystal, and black arrows indicate surface steps which can be observed every 1−2 nm.

$SrCO_3$ displays a strong peak at 148 cm^{-1}, our experimental evidence suggests that the peak at 146 cm^{-1} observed in MSS-1 STO belongs to $SrCO_3$ and not to first-order Raman scattering from vibrational modes arising from tetragonal domains present in the STO nanocubes. The presence of tetragonal domains cannot, however, be ruled out. Although a very weak shoulder at 224 cm^{-1} is observed in the spectra of MSS-1, MSS-2, and HTS STO collected under low vacuum, a band at this Raman shift is clearly noticeable in the spectra of MSS-1 and MSS-2 STO acquired under ambient conditions. This band is assigned, tentatively, to the B_{2g} phonon of the tetragonal phase.

The appearance of Raman bands corresponding to IR active polar modes at temperatures well above 110 K, where the bulk crystalline structure is cubic, demonstrates the local loss of inversion symmetry. Similar spectral features have been observed for STO sintered ceramics,[19] STO thin films (27−2300 nm thick),[5,29–33] and STO nanocubes with an average size of 80 nm,[16] as well as for the mixed systems $Ba_xSr_{1-x}TiO_3$,[34] and $Ca_xSr_{1-x}TiO_3$.[27,35] Nominally pure samples

(29) Merkulov, V. I.; Fox, J. R.; Li, H.-Ch.; Si, W.; Sirenko, A. A.; Xi, X. X. *Appl. Phys. Lett.* **1998**, *72* (25), 3291–3293.
(30) Sirenko, A. A.; Akimov, I. A.; Fox, J. R.; Clark, A. M.; Li, H.-Ch.; Si, W.; Xi, X. X. *Phys. Rev. Lett.* **1999**, *82* (22), 4500–4503.
(31) Gupta, S.; Katiyar, R. S. *J. Raman Spectrosc.* **2001**, *32*, 885–891.
(32) Hilt Tisinger, L.; Liu, R.; Kulik, J.; Zhang, X.; Ramdani, J.; Demkov, A. A. *J. Vac. Sci. Technol., B* **2003**, *21* (1), 53–56.
(33) Du, Y. L.; Chen, G.; Zhang, M. S. *Solid State Commun.* **2004**, *130*, 577–580.
(34) Tenne, D. A.; Soukiassian, A.; Zhu, M. H.; Clark, A. M.; Xi, X. X.; Choosuwan, H.; He, Q.; Guo, R.; Bhalla, A. S. *Phys. Rev. B* **2003**, *67*, 012302.

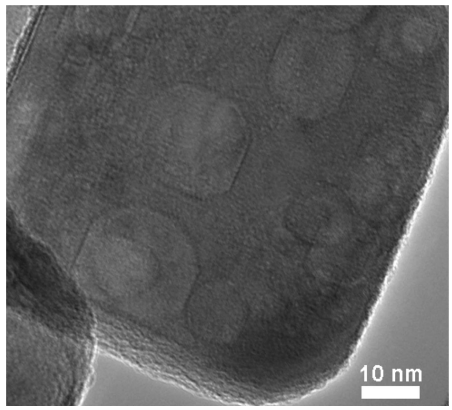

Figure 6. High-resolution TEM image of a single HTS STO nanocube. A significant number of square-shaped structures can be clearly seen; notice their lower contrast.

of the incipient ferroelectric $KTaO_3$,[36,37] and Li-[38] or Nb-[39] substituted $KTaO_3$ single crystals also show first-order Raman lines in their spectra. The loss of inversion symmetry has been ascribed to point defects such as impurities[16,25,36,40] and oxygen vacancies;[16,29–31,33,34,37] as these are common defects in perovskites, they are likely to be present in our nanocubes. The activation of first-order Raman scattering in STO nanocubes suggests that the concentration of these point defects is significantly higher than in the SSR sample. In the case of MSS nanocubes, the concentration of oxygen vacancies is expected to be higher than in the SSR sample, because of the reducing atmosphere that arises from the decomposition of SrC_2O_4 that yields CO and CO_2.[41] Along with a higher concentration of oxygen vacancies, other point defects such as cation vacancies or neutral vacancy pairs may also be present. The absence of inversion symmetry gives rise to polar regions that interact with polar phonons inducing their optical activity; the size of these polar domains was found to increase upon cooling.[36,40] Petzelt and co-workers[19] also suggested that frozen dipoles present in grain boundaries of STO ceramics induce the polar phase in the grain bulk, removing the inversion symmetry, thereby allowing scattering from polar phonons; a free surface can act similarly. This effect is expected to become more significant as the surface-to-volume ratio of the particles increases, i.e., as the particle size gets smaller.[5] It should be pointed out that unlike the case of thin films, where the lattice mismatch between the film and the substrate acts as an external source of strain, thereby lowering the film lattice symmetry,[30,31] the nanostructures presented in this work are free-standing and therefore, there are no sources of strain other than point defects and surfaces.

According to previous investigations,[30,31,33,35] the activation of the silent TO3 and nonpolar LO3 phonon indicates long-range distortions of the cubic structure. From this perspective, the presence of peaks corresponding to these phonons in the Raman spectrum of HTS STO at room temperature, as well as their intensity, which is noticeably higher than in MSS STO nanoparticles (see Figures 7b−d and 8), suggests that acentric regions occupy a significantly larger fraction of the total volume of the sample in HTS STO nanocubes. The enhancement of local symmetry distortions in these nanoparticles may be ascribed to two structural factors: First, a concentration of point defects greater than in nanoparticles obtained via molten salt. Because HTS STO nanoparticles were obtained under strong alkaline condition, it is likely that residual hydroxyl groups were incorporated in the perovskite oxygen sublattice during the crystal growth process; a similar phenomenon has been observed for $BaTiO_3$ (BTO) nanoparticles prepared using solution-based synthesis.[42–44] As a result of the substitution of OH^- for O^{2-}, other point defects such as cation vacancies or neutral vacancy pairs may also be created to maintain the electroneutrality of the perovskite structure. In addition, the presence of nanosized cavities in HTS STO crystals, not observed in MSS nanoparticles, which constitute surfaces within the nanocrystals, is an additional source of frozen dipoles that lower the grain bulk symmetry; their effect is analogous to polar grain boundaries and pores in STO ceramics[19] and thin films,[5] respectively.

The presence of polar domains in our STO nanocubes is strongly supported by the pronounced Fano-like shape of the peak corresponding to the TO2 polar phonon; this kind of asymmetry has been observed previously in STO ceramics[19] and thin films,[30,31,33] $Ba_xSr_{1-x}TiO_3$ thin films,[34] and $Ca_xSr_{1-x}TiO_3$ ceramics.[27,35] The Fano asymmetry arises from the coherent interference of a discrete phonon and a broad continuum of excitations.[45] Fano-like shapes are fitted using the following equation

$$I(\omega) = A\frac{[q + E(\omega)]^2}{1 + E^2(\omega)} + C \quad (1)$$

where $E(\omega)$ is a reduced frequency given by

$$E(\omega) = 2(\omega - \omega_0)/\Gamma \quad (2)$$

and $I(\omega)$ is the intensity, A is the amplitude, ω_0 is the phonon frequency, q is the asymmetry parameter, Γ is the full width at half-maximum, and C is a constant that accounts for the background. Lorentzian, i.e., symmetric, peak shapes correspond to $q \rightarrow \infty$. Figure 9 shows the fitting of the 176 cm^{-1} peak at room temperature for MSS-1 STO.

The temperature dependence of the asymmetry parameter q for MSS-1, MSS-2, and HTS STO samples is plotted in Figure 10. In theory, q is inversely proportional to the density of states for the continuum of excitations (ρ_0) at ω_0. As ρ_0

(35) Ranson, P.; Ouillon, R.; Pinan-Lucarre, J.- P.; Pruzan, Ph.; Mishra, S. K.; Ranjan, R.; Pandey, D. *J. Raman Spectrosc.* **2005**, *36*, 898–911.
(36) Uwe, H.; Lyons, K. B.; Carter, H. L.; Fleury, P. A. *Phys. Rev. B* **1986**, *33* (9), 6436–6440.
(37) Jandl, S.; Grenier, P.; Boatner, L. A. *Ferroelectrics* **1990**, *107*, 73–77.
(38) Prater, R. L.; Chase, L. L.; Boatner, L. A. *Phys. Rev. B* **1981**, *23* (11), 5904–5915.
(39) Prater, R. L.; Chase, L. L.; Boatner, L. A. *Phys. Rev. B* **1981**, *23* (1), 221–231.
(40) Uwe, H.; Yamaguchi, H.; Sakudo, T. *Ferroelectrics* **1989**, *96*, 123–126.
(41) Rørvik, P. M.; Lyngdal, T.; Sæterli, R.; van Helvoort, A. T. J.; Holmestad, R.; Grande, T.; Einarsrud, M.-A. *Inorg. Chem.* **2008**, *47* (8), 3173–3181.
(42) Wada, S.; Tsurumi, T.; Chikamori, H.; Noma, T.; Suzuki, T. *J. Cryst. Growth* **2001**, *229*, 433–439.
(43) Vivekanandan, R.; Philip, S.; Kutty, T. R. N. *Mater. Res. Bull.* **1986**, *22*, 99–108.
(44) Vivekanandan, R.; Kutty, T. R. N. *Powder Technol.* **1989**, *57*, 181–192.
(45) Fano, U. *Phys. Rev.* **1961**, *124* (6), 1866–1878.

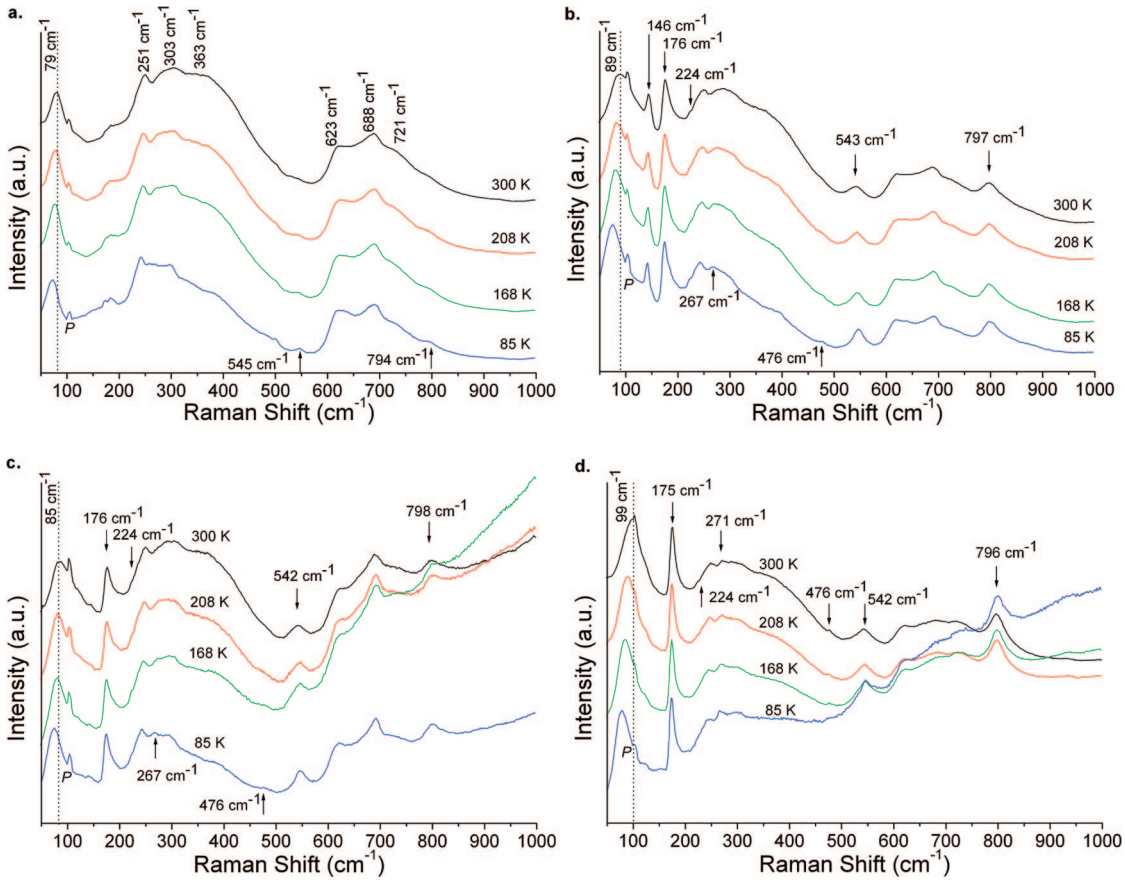

Figure 7. Raman spectra of: (a) SSR, (b) MSS-1, (c) MSS-2, and (d) HTS STO collected under low vacuum condition (0.1 Torr) over the temperature range 85−300 K. First-order Raman peaks are denoted by arrows at their corresponding frequencies; their assignment is discussed in the text. The dotted line indicates the Raman shift of the low-frequency band at 300 K. The sharp peak labeled *P*, present over the whole range of temperatures, corresponds to a plasma line.

Table 1. Room-Temperature Zone-Center Phonon Frequencies (in cm^{-1}) and Their Assignments for $SrTiO_3$

phonon branch	symmetry	INS[a]	IR[b]	HRS[c]
TO1	T_{1u} (IR active)	92	93	88
LO1		169	171	175
TO2	T_{1u} (IR active)	169	176	175
LO2		265		266
TO3	T_{2u} (silent)	265		266
LO3		457	472	474
TO4	T_{1u} (IR active)	547	548	545
LO4		823	795	795

[a] Inelastic neutron scattering data from ref 18. [b] Infrared reflectivity data from ref 19. [c] Hyper-Raman spectroscopy data from ref 20.

→ 0, $q \rightarrow \infty$ and the peak shape becomes Lorentzian. The TO2 phonon line displays a more asymmetric character for MSS than for HTS STO nanocubes in the entire range of temperatures. For the former, q does not exhibit significant changes with temperature. This differs from the result of Banerjee and co-workers[16] who reported a significant increase of q as the temperature was raised, followed by a decrease above ca. 320 K. In contrast, a monotonous decay of q with increasing temperature was reported by Sirenko[30] and Gupta et al.[31] in STO thin films. Both authors observed a striking similarity between the temperature dependence of the dielectric constant and the asymmetry parameter. The variation of q with temperature for HTS STO nanocubes is the opposite of what has been reported for STO thin films, making an investigation of the dielectric properties of these nanocubes very intriguing.

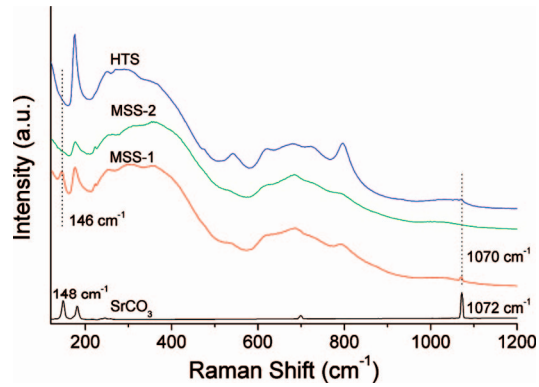

Figure 8. Raman spectra of $SrCO_3$, MSS-1, MSS-2, and HTS STO recorded at 300 K in ambient condition. Peaks corresponding to $SrCO_3$ are denoted by dotted lines. Notice that spectra of $SrCO_3$-free samples do not exhibit a peak at 146 cm^{-1}. All the spectra are plotted in the same scale, offset for clarity.

In light of the above results, the low frequency region of the spectrum deserves careful examination. As mentioned earlier, in the case of SSR STO the band at 79 cm^{-1} can be assigned to second-order scattering on the basis of symmetry arguments. However, for STO nanocubes, where strong first-order Raman activity is observed at room temperature, a band corresponding to the TO1 mode is expected to appear in this region concurrently with other IR active TO phonons. The TO1 "soft" phonon has been shown to drive the ferroelectric

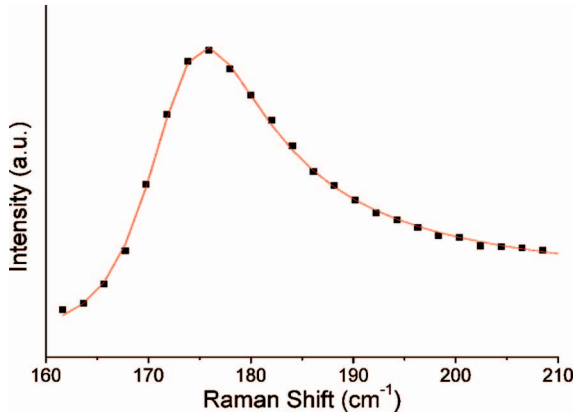

Figure 9. Fano line shape corresponding to the TO2 phonon for MSS-1 STO at 300 K. Solid symbols represent experimental data; the solid line represents the fit to the Fano profile. The fitting parameters are: $\omega_0 = 173.08 \pm 0.11$ cm^{-1}, $\Gamma = 14.08 \pm 0.29$ cm^{-1}, $q = 2.75 \pm 0.05$, and $A = 0.035 \pm 0.001$.

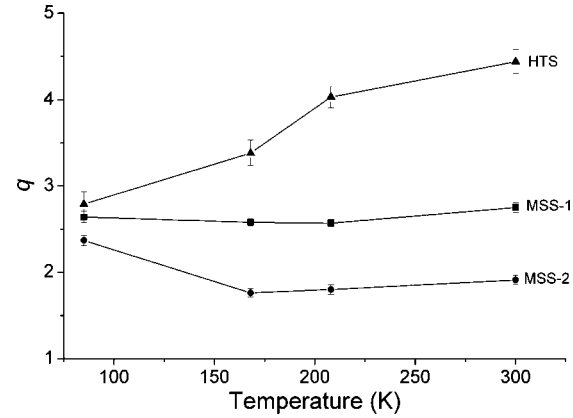

Figure 10. Temperature dependence of the asymmetry parameter q for MSS-1, MSS-2, and HTS STO nanocubes. Solid lines connecting points are guides for the eye.

instability of the perovskite lattice, responsible for the incipient ferroelectricity exhibited by STO.[46] From Figures 7b-d we notice that for MSS STO nanocubes the low-frequency band shifts from 89 to 75 cm^{-1} (-14 cm^{-1}) for MSS-1, and from 85 to 75 cm^{-1} (-10 cm^{-1}) for MSS-2 STO. Finally, for HTS STO nanoparticles the shift is even more pronounced: from 99 to 78 cm^{-1} (-21 cm^{-1}). For all three samples, the intensity of this low-frequency band increases significantly upon cooling, in contrast to SSR STO where no significant changes are noticeable. Sirenko et al.[30] observed first-order Raman scattering in STO thin films arising from TO2, TO3, and TO4 phonons, but no features corresponding to the TO1 phonon were reported. Instead, a broad maximum around 90 cm^{-1} was found between 5 and 100 K. Similarly, Du et al.[33] observed a broadband at 92 cm^{-1} that became more intense upon cooling. Ranson and co-workers[35] observed a similar band in polycrystalline $Ca_xSr_{1-x}TiO_3$ samples. These authors suggested that the appearance of this band is connected to the presence of defect-induced polar microregions. In addition, Ostapchuk et al. reported that the temperature-dependence of the TO1 phonon frequency differs for STO thin films exhibiting different microstructural features.[5] Similarly, our experimental data show that the phonon dynamics in the low frequency region of the spectrum differs for different STO nanocubes, although definitive spectral features cannot be attributed to the TO1 phonon. Results from previous investigations suggest that these differences in the behavior of the band below 100 cm^{-1} arise from polar domains that occupy a significantly large fraction of the total volume of the STO nanocubes. In view of the important role played by the "soft" TO1 phonon in determining the dielectric properties of STO, the low frequency region ($10-100$ cm^{-1}) is worth further investigation.

Conclusions

STO polycrystalline ceramics were prepared using three different synthetic approaches: solid-state reaction, molten salt, and sol-precipitation coupled with hydrothermal synthesis. Conventional solid-state reaction yielded a polycrystalline product of uncontrolled morphology, whereas sol-precipitation coupled with hydrothermal synthesis and molten salt yielded single-crystalline STO nanocubes with average edge lengths of 60 and 120 nm, respectively.

Our Raman data showed that the local crystal structure and lattice dynamics of each of these STO samples strongly depend on the synthetic route employed. Specifically, the observation of strong first-order Raman activity in STO nanocubes at room temperature suggested the presence of polar domains. The presence of first-order Raman features should be of interest for materials chemists working on the development of electronic materials, as their strength is directly related to the volume fraction of the nanocrystal occupied by polar domains, which is, according to our findings, dependent on the synthetic method employed to prepare the nanoparticles.

Of special significance are the differences observed in the temperature dependence of the low frequency spectral features, as these are likely to have implications for the dielectric properties of these nanostructures. In order to gain further insight into their ferroelectric or incipient ferroelectric behavior, Raman scattering measurements of these STO nanocubes over the frequency range $10-100$ cm^{-1} and extended down to liquid He temperatures, as well as temperature-dependent studies of their dielectric response, would definitely be worthwhile.

Acknowledgment. This work was supported by the Chemical Sciences, Geosciences and Biosciences Division, Office of Basic Energy Sciences, Office of Science, U.S. Department of Energy (Award DE-FG02-03-ER15457).This work made use of the J. B. Cohen X-ray Diffraction Facility supported by the MRSEC program of the National Science Foundation (DMR-0520513) at the Materials Research Center of Northwestern University.The electron imaging and diffraction work was performed in the EPIC facility of NUANCE Center at Northwestern University. NUANCE Center is supported by NSF-NSEC, NSF-MRSEC, Keck Foundation, the State of Illinois, and Northwestern University.

Supporting Information Available: Electron energy loss spectroscopy (EELS) thickness mapping of a single $SrTiO_3$ nanocube obtained via a sol-precipitation−hydrothermal treatment procedure (PDF). This information is available free of charge via the Internet at http://pubs.acs.org.

(46) Cochran, W. *Adv. Phys.* **1960**, *9* (36), 387–423.

CM801192T